Evolving Biofilm Morphology Controls Microplastic Transport in Porous Media

Zhongyu Shi[1] and Yinuo Noah Yao*[1]

[1]Zachry Department of Civil and Environmental Engineering, Texas A & M University, College Station, TX 77843, USA

*Email: yyao@tamu.edu

Abstract

Microplastics (MPs) entering soils and subsurface environments interact with biofilms that continually reshape pore geometry and local flow pathways, yet biofilm effects on MP transport are only studied under fixed conditions. Here, we used a saturated microfluidic porous medium to directly image biofilm development and track fluorescent polyethylene MPs at different stages of biofilm growth. Changes in biofilm morphology were quantified from transmitted-light intensity distributions, while particle trajectories were used to determine microplastic retention times and trapped fractions. Streamer-rich biofilms resulted in spatially distributed MP pathways, broader retention-time distributions, and greater particle trapping. In contrast, the bioclogged porous medium resulted in connected preferential flow paths (PFPs) that enabled rapid MP transport and reduced particle-biofilm interactions. Across all conditions, the streamer-associated component weight was positively correlated with both the mean normalized retention time (Spearman $r_s = 0.92$, $p = 0.0002$) and trapped fraction (Spearman $r_s = 0.87$, $p = 0.0012$). In contrast, neither the mean normalized retention time nor the trapped fraction showed a significant relationship with the total biofilm-associated optical fraction. These results show that MP transport depends strongly on biofilm morphology rather than biofilm accumulation alone. Biofilm development can therefore shift MP transport from spatially distributed and delayed transport under streamer-rich conditions to rapid transport through a focused PFP. This morphology-dependent behavior, therefore, imposes significant challenges in predicting MP retention and downstream migration in biologically active porous media.

Keywords

Microfluidics, lab-on-a-chip, streamers, bioclogging, preferential flow paths, subsurface, particle tracking

Introduction

Microplastics (MPs; typically $< 5\,\text{mm}$) are widespread environmental contaminants because of high plastic production, low recycling rates, and their resistance to degradation.[1–3] MPs have been detected in terrestrial environments, such as wastewater-impacted soils and agricultural lands.[4–6] Treated wastewater, sewage sludge, and landfill leachate are important pathways that release MPs into subsurface environments.[4,7,8] Additionally, persistent MPs can further fragment into nanoplastics, which have been shown to be taken up and translocated by crops.[9] Without understanding how MPs are transported and retained after entering subsurface porous media, predicting their persistence and long-term fate remains challenging.

Most previous studies have focused on the physical and chemical effects on mobility.[7,10–12] For example, column experiments have shown that MP retention increases at lower flow rates.[11,13] To predict MP transport, particle-surface interactions have been modeled using approaches adapted from colloid transport, such as DLVO theory.[7,12] Nizzetto *et al.*[10] have incorporated hydrologic, soil erosion, and sediment transport processes to predict MP mobility at larger scales, showing that MP transport depends strongly on particle properties, porous-medium properties, and hydrodynamic conditions.[12,14]

However, most of these studies treat the porous medium as static, with fixed pore geometry and surface properties. In natural systems, microorganisms are ubiquitous, and biofilm growth can modify surface properties, pore geometry, and local flow conditions.[15–19] These changes can, in turn, alter MP transport in porous media. He *et al.*[20] showed that *E. coli* biofilm growing in a sand filtration system enhanced MP deposition by altering surface interactions. Other studies have also reported enhanced particle attachment and retention in biofilm-colonized porous media.[21,22] In contrast, Wei *et al.*[23] showed that biofilm growth on MP surfaces can promote particle mobilization under subcritical shear by increasing hydrodynamic lift forces.

At the same time, biofilm morphology changes during growth and can produce structures with distinct hydrodynamic characteristics.[15,16] For example, biofilms can form streamers that contain bacterial cells embedded in extracellular polymeric substances (EPS) and extend into the flowing pore space.[24,25] These filamentous structures provide an extended biofilm-fluid interface.[26–28] In contrast, biofilms can result in bioclogging of the pore network and redistribute flow into preferential flow paths (PFPs).[15,17,18] However, the effects of streamer formation and subsequent PFP development on MP transport remain poorly understood.

Quantifying the temporal evolution of biofilm morphology remains challenging. Optical coherence tomography (OCT) and confocal laser scanning microscopy (CLSM) can resolve three-dimensional biofilm structures, but repeated imaging over extended growth periods is limited by imaging time and field of view.[29–32] Microfluidic platforms[19,33,34] coupled with microscopy provide a transparent system in which biofilm development and particle transport can be monitored within the same pore space under controlled hydrodynamic conditions. This enables individual MPs to be tracked as biofilm morphology evolves. Despite these capabilities, the temporal relationship between pore-scale biofilm morphology and MP transport remains unclear.[23,35]

In this study, we investigate the effects of evolving biofilm morphology on MP transport in saturated porous media. We use a microfluidic porous medium to directly image biofilm development and track individual MPs at different stages of biofilm growth. We quantify the fraction of trapped MPs and the retention time of non-trapped MPs and relate these transport behaviors to changes in biofilm morphology. Our results show that the effects of biofilm on MP transport vary during biofilm development. Streamer-rich biofilms increase MP retention time and trapping, whereas continued biofilm growth results in PFP formation that redirects particles through connected open pore spaces and leads to more rapid transport. These results demonstrate that biofilm morphology, rather than biofilm alone, is an important control on MP transport in porous media.

Materials and Methods

Bacterial culture conditions

We performed the experiments using *Bacillus subtilis* 168, a well-studied Gram-positive soil bacterium with robust biofilm-forming abilities.[36,37] Frozen glycerol stocks of *B. subtilis* 168 were stored at −80 °C in 15% (v/v) glycerol. To obtain isolated colonies, a small amount of frozen stock was transferred using a sterile inoculation loop, streaked onto LB plates containing 1.5% agarose (Thermo Fisher Scientific), and incubated at 37 °C for 16 hours. We prepared the bacterial culture by inoculating colonies from the agar plates into 100 mL of autoclaved modified LB medium containing 2 g of Luria Bertani (LB) broth powder (Thermo Scientific) and 2 mL of mineral stock (9.9 g/L $MnCl_2 \cdot 4\,H_2O$, TCI America; 66.15 g/L $CaCl_2 \cdot 2\,H_2O$, Thermo Fisher Scientific), with deionized water added to a final volume of 100 mL. Calcium and manganese ions were added to promote biofilm formation.[38]

The bacterial culture was incubated for 12 hours at 30 °C with shaking at 200 rpm (NEWTRY). Then, 0.1 mL of the *B. subtilis* culture was transferred into 100 mL of fresh modified LB medium and incubated

under the same conditions until the optical density at 600 nm (OD_{600}) reached 0.1, measured using a UV spectrophotometer (VWR, P9 UV/Visible, Double-beam). Finally, 10 mL of the bacterial suspension was collected and immediately used for the subsequent microfluidic experiments.

Microfluidic device design and fabrication

Design. Following Kurz *et al.*,[15] we designed a microfluidic device with inlet, porous, and outlet regions to mimic a uniform porous medium with a porosity of 0.77. The porous region contains cylindrical pillars with a diameter of $D = 150\,\mu m$ arranged in a staggered pattern, with a center-to-center spacing of $2D$ between neighboring pillars (Figure 1(a)). The porous region had dimensions of $22\,mm \times 4.05\,mm \times 0.1\,mm$.

Fabrication. The microfluidic device was fabricated using standard soft lithography techniques.[33] A photomask was fabricated using a maskless aligner system (Heidelberg MLA 150), and the microchannel mold was prepared on a silicon wafer spin-coated with SU-8 2050 negative photoresist (Kayaku Advanced Materials) and patterned using an EVG 610 double-sided mask aligner. Polydimethylsiloxane (PDMS; Sylgard 184 Silicone Elastomer Kit, Dow Corning) was prepared using a 10:1 base-to-curing-agent ratio, followed by mixing, degassing, casting onto the patterned wafer, and curing at 85 °C for 1 h. The cured PDMS layer was then removed from the mold, trimmed to the desired size, and irreversibly bonded to a glass slide using oxygen plasma treatment (Tegal Plasmaline 421 asher). The inlet and outlet were connected to silicone tubes after being cut by a biopsy punch (MedBlades, 1.5 mm) (Figure 1(b)).

Biofilm growth and imaging

Pretreatment. The microfluidic device was rinsed with 75% ethanol (Fisher Scientific) at 0.5 mL/h using syringe pumps (Pump 11 Elite, Harvard Apparatus) for 24 hours for sterilization and removal of residual air bubbles. The device was subsequently rinsed with deionized water to remove residual ethanol. Additionally, we installed a sterile syringe filter (Membrane Solutions) with a pore size of 1.2 µm between the syringe and the microfluidic device to prevent biofilm contamination in the upstream silicone tubing and subsequent clogging within the upstream tubing.

Inoculation. The device was rinsed with 2 mL of modified LB medium at a flow rate of 10 mL/h. Then, 10 mL of bacterial solution was rapidly injected into the microfluidic device through the outlet. The microfluidic device was then maintained under near-no-flow conditions for 3 hours to allow initial surface attachment.[15,33] Here, considering the pressure imbalance associated with fluid levels in the syringe pump and microfluidic device, we adjusted the syringe flow rate until no flow was visible under the microscope, resulting in a compensating flow rate of 0.082 mL/h.

Growth conditions and monitoring. We placed the microfluidic device inside a stage-top incubator (Tokai Hit USA Inc.) and maintained it at 30 °C. During growth, modified LB medium was continuously injected at a flow rate of 0.5 mL/h. Biofilms were monitored using a digital camera (Orea) mounted on an inverted confocal microscope (Ti-Eclipse 2, Nikon) at 2× magnification and a frame rate of 0.1 fps. Since the entire porous region could not be captured within a single field of view, the microscope stage was programmed to alternate between two adjacent positions during each imaging cycle. The resulting images were stitched using Nikon software to obtain the complete porous region at a resolution of 13,500 × 2,500 pixels.

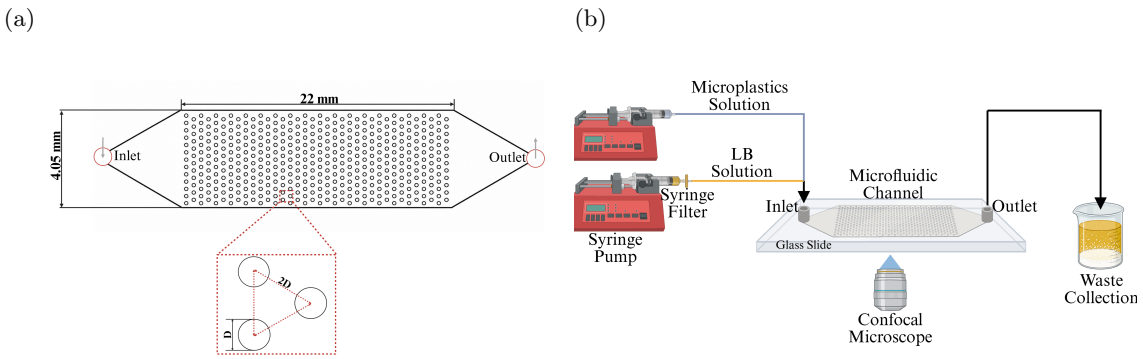

Figure 1: Microfluidic porous-medium geometry and experimental setup. (a) Device geometry with staggered cylindrical pillars of diameter $D = 150\,\mu\text{m}$ and center-to-center spacing $2D$. (b) Experimental setup for biofilm growth, MP injection, and imaging. A flow rate of $Q = 0.5\,\text{mL/h}$ was used during biofilm growth and MP transport measurements.

Microplastic suspension and injection

In this study, we used fluorescent green polyethylene microspheres (Cospheric LLC) with a density of $1000\,\text{kg/m}^3$ and a particle diameter of 27–30 µm as model microplastics. The fluorescent signal allowed the microspheres to be distinguished from the biofilm during imaging and subsequently tracked to quantify microplastic transport.

Preparation. To minimize particle aggregation and adhesion to the PDMS surface during injection, we prepared the microplastic suspension using 5 mL of modified LB medium containing 1 g/L of Tween 20 surfactant (Sigma-Aldrich). Since polyethylene microspheres can interact with neighboring particles and the PDMS surface, they may aggregate and resist flow. We therefore added Tween 20 to reduce these non-specific interactions and better isolate the effects of biofilm morphology on microplastic transport. The suspension was centrifuged at 10,000 rpm for 5 min using a VWR high-speed microcentrifuge and immediately drawn into a sterile syringe fitted with a 25 G needle for MP injection. A fresh suspension was prepared before each injection to maintain consistent particle dispersion and minimize non-specific attachment.

Injection. For each microplastic injection, we paused the injection of modified LB medium for 5 min. The syringe containing the microplastic suspension was inserted into the silicone tubing near the device inlet.

After flow resumed at 0.5 mL/h, microplastic transport was recorded for 10 min at 4 fps with an image resolution of 256 × 256 pixels. We deliberately chose a lower image resolution, allowing a higher frame rate needed to resolve microplastic motion. MP tracking was performed within a single observation window spanning 8.5 mm in the streamwise direction, and no image stitching was used. Two sequential MP injections were performed at each observation time within the same window to characterize transport under the same stage of biofilm development. After the microplastic injections, modified LB medium without microplastics was continuously supplied, and biofilm monitoring was resumed.

Image analysis

Quantification of biofilm morphology

Following Kurz *et al.*,[15,16] we related changes in transmitted-light intensity to biofilm growth using the Lambert-Beer law such that

$$\ln I_s(\mathbf{x},t) = -\epsilon \cdot c(\mathbf{x},t) \cdot h, \tag{1}$$

where $I_s(\mathbf{x},t) = \hat{I}_s(\mathbf{x},t)/\mathcal{I}(\mathbf{x})$ is the normalized transmitted light intensity at location $\mathbf{x}$ and time t, $\hat{I}_s(\mathbf{x},t)$ is the measured light intensity from microfluidic images, $\mathcal{I}(\mathbf{x}) = \hat{I}_s(\mathbf{x},t=0)$ refers to the background reference intensity, ϵ is the effective absorption coefficient of the biofilm, $c(\mathbf{x},t)$ is the local concentration of light-absorbing biofilm material, and h is the height of the microfluidic device. Since ϵ was not independently measured and the images approached the detection limit in optically dense regions, $c(\mathbf{x},t)$ could not be determined quantitatively. We therefore used $I_s(\mathbf{x},t)$ as an optical indicator of biofilm morphology rather than a direct measurement of biofilm density. For each time point, the normalized intensity field $I_s(\mathbf{x},t)$ was converted into an intensity distribution. The resulting distributions were generally multimodal as biofilm developed, showing the coexistence of regions with different optical characteristics.

The intensity distributions were fitted using four Gaussian components such that

$$f(I_s,t) = \sum_{k=1}^{K} g_k(I_s,t), \qquad K = 4, \tag{2}$$

where g_k is the kth Gaussian component, defined by an amplitude $a_k(t)$, mean intensity $\mu_k(t)$, and standard

deviation $\sigma_k(t)$. Four components were used to consistently resolve the dominant intensity modes observed throughout biofilm development. The Gaussian parameters were obtained using differential evolution by minimizing the mean squared error (MSE) between the measured and fitted intensity distributions such that

$$\mathrm{MSE}(t) = \frac{1}{N_b} \sum_{j=1}^{N_b} \left[\hat{f}(I_{s,j}, t) - f(I_{s,j}, t) \right]^2, \tag{3}$$

where N_b is the number of intensity bins, $\hat{f}(I_{s,j}, t)$ is the measured intensity distribution at bin j, and $f(I_{s,j}, t)$ is the corresponding fitted value.

A two-stage fitting procedure was then applied to prevent the Gaussian components from shifting between intensity modes over time. In the first stage, the four components were fitted without constraints, yielding $\mu_k(t)$ for each component k. When the contribution of a component became small, its fitting curve shifted substantially from its average range. We therefore calculated the temporal mean of $\mu_k(t)$ from the first-stage fits as

$$\overline{\mu}_k = \frac{1}{N_t} \sum_{i=1}^{N_t} \mu_k(t_i), \tag{4}$$

where N_t is the number of analyzed time points. In the second stage, $\mu_k(t)$ was constrained within $\overline{\mu}_k \pm 0.05$ for each component. The final constrained fits generally resulted in $\mathrm{MSE} < 10^{-4}$.

Once fitted, the relative contribution of each optical component was quantified from the integrated area of its fitted Gaussian distribution. Specifically,

$$S_k(t) = \int g_k(I_s, t)\, dI_s, \tag{5}$$

and the corresponding component weight was defined as

$$W_k(t) = \frac{S_k(t)}{\sum_{j=1}^{K} S_j(t)}, \tag{6}$$

such that $\sum_{k=1}^{K} W_k(t) = 1$. The Gaussian components were associated with different biofilm morphologies by comparing their characteristic intensity ranges with the corresponding microfluidic images. For the remainder of this paper, we refer to the component weights as $W_1 \equiv W_v$ for void space, $W_2 \equiv W_s$ for

streamers, and $W_3 \equiv W_{b,1}$ and $W_4 \equiv W_{b,2}$ for two biofilm-associated optical components with progressively lower characteristic intensities. The temporal evolution of these weights was then used to quantify changes in biofilm morphology during growth.

Microplastic tracking and transport analysis

We quantified microplastic transport in the microfluidic device using a modified particle tracking algorithm adapted from Ouellette *et al.*,[39] with additional treatment for particle clusters formed when multiple microplastics accumulated at the same location. Individual-particle detections were matched across frames using a global one-to-one assignment based on the Hungarian algorithm. Figure S2 shows a schematic of the particle tracking workflow.

For each individual particle, the position in the subsequent frame was predicted from its current position and estimated velocity as

$$\widetilde{\mathbf{x}}_i^{n+m+1} = \mathbf{x}_i^n + (m+1)\widetilde{\mathbf{v}}_i^n \Delta t, \tag{7}$$

where $\widetilde{\mathbf{x}}_i^{n+m+1}$ is the predicted position of the ith particle at frame $n+m+1$, $\mathbf{x}_i^n$ is its position at frame n, $\widetilde{\mathbf{v}}_i^n$ is the estimated particle velocity, $\Delta t = 0.25\,\mathrm{s}$ is the time interval between adjacent frames, and m is the number of missing frames ($m = 0$ for matching between consecutive frames). Particle positions were defined by the centroid coordinates of the detected fluorescent contours. For a particle i in frame n and a candidate particle j in frame $n+m+1$, the matching cost was defined as

$$C_{ij} = w_p d_{ij}^{\mathrm{pred}} + w_d d_{ij}^{\mathrm{disp}}, \tag{8}$$

where

$$d_{ij}^{\mathrm{pred}} = \left\| \mathbf{x}_j^{n+m+1} - \widetilde{\mathbf{x}}_i^{n+m+1} \right\|_2, \qquad d_{ij}^{\mathrm{disp}} = \left\| \mathbf{x}_j^{n+m+1} - \mathbf{x}_i^n \right\|_2. \tag{9}$$

The weighting coefficients were set to $w_p = 0.6$ and $w_d = 0.4$, giving slightly greater weight to the predicted particle position. The resulting cost matrix was solved using the Hungarian algorithm to obtain the one-to-one assignment that minimized the total matching cost for each frame transition. Candidate pairs were excluded when the frame-to-frame displacement exceeded 2.66 mm (80 pixels). This displacement limit was

selected based on the tracking-sensitivity analysis and is consistent with the rapid particle transport observed under PFP conditions. The retention-time PDFs for all cases across the tested matching distances are shown in Figure S3 of the Supporting Information.

To account for temporary detection failures, unmatched trajectories were retained for up to two consecutive missing frames. For gap recovery ($m = 1$ or 2), the maximum allowable displacement was scaled to $(m + 1)d_{\max}$ to account for the longer elapsed time. Candidate detections were then evaluated using the same prediction-based matching procedure described above. Particles detected in the immediately preceding frame were matched first, followed by previously unmatched trajectories, to reduce incorrect reconnections across missing frames. When a trajectory was successfully recovered, the detections were treated as part of the same continuous trajectory, and the missing interval was included in the retention time. The particle velocity was then updated from the displacement between the last observed and recovered positions over the full elapsed interval $(m + 1)\Delta t$.

Particle clusters were handled before the remaining individual-particle detections were matched because a single fluorescent contour could represent multiple MPs, and clustered particles were commonly retained at the same location. For each detected cluster, we estimated the number of particles in the kth cluster as

$$\widehat{N}_{c,k}(t) = \frac{A_{c,k}(t)}{\overline{A}_p}, \tag{10}$$

where $\widehat{N}_{c,k}(t)$ is the estimated number of particles in the kth cluster, $A_{c,k}(t)$ is the contour area of the cluster at time t, and $\overline{A}_p$ is the mean contour area of an isolated particle. Following the first-in–first-out (FIFO) sequence, when the estimated particle number increased, newly arriving particles were added to the cluster. When it decreased, the particle that entered earliest was assumed to leave first, and its retention time was recorded. Cluster-associated detections were then removed from the matching pool, and the remaining individual particles were matched using the procedure described above. Manual validation showed 90.2% overall agreement between reconstructed and manually inspected trajectories, ranging from 81.5% under rapid PFP transport to 100% under streamer-rich conditions (Table S1, Supporting Information).

The reconstructed trajectories and corresponding retention times were used to classify MP transport. Particles that exited the observation region were classified as non-trapped. Particles remaining in the final frame were classified as trapped only when their retention time exceeded 2.5 s. This threshold was used to exclude particles entering near the end of the observation period, for which insufficient time remained to distinguish temporary residence from persistent trapping. Shorter trajectories were excluded because particles entering near the end of the observation period could not be reliably distinguished from trapped

particles. For each non-trapped MP, the retention time τ_r was defined as the time that the particle remained within the observation region. We normalized τ_r using a characteristic advective timescale associated with transport through a PFP. Kurz *et al.*[15] reported a maximum mean PFP width of approximately one-half of the pore size in a comparable microfluidic porous medium. Using $W_{\mathrm{PFP}} = D/2$, the characteristic PFP velocity and transit time were estimated as

$$u_{\mathrm{PFP}} = \frac{Q}{W_{\mathrm{PFP}} H}, \qquad \tau_{\mathrm{PFP}} = \frac{L}{u_{\mathrm{PFP}}} = \frac{L W_{\mathrm{PFP}} H}{Q}, \tag{11}$$

where $L = 8.5\,\mathrm{mm}$ is the length of the particle-tracking region, $H = 0.1\,\mathrm{mm}$ is the device depth, and $Q = 0.5\,\mathrm{mL/h}$ is the flow rate during MP transport. This gives $\tau_{\mathrm{PFP}} \approx 0.46\,\mathrm{s}$ under the present flow condition. This estimate was used as a characteristic timescale for rapid PFP transport rather than as a direct measurement of the local velocity. The complementary cumulative distribution function (CCDF) of non-trapped MPs was calculated as

$$S(\tau^*) = P(\tau_r^* > \tau^*), \tag{12}$$

where $\tau_r^* = \frac{\tau_r}{\tau_{\mathrm{PFP}}}$. For trapped MPs, we computed the trapped fraction as

$$f_t = \frac{N_t}{N_{\mathrm{classified}}}, \tag{13}$$

where N_t is the number of trapped MPs and $N_{\mathrm{classified}}$ is the total number of classified trapped and non-trapped MPs. Spearman rank correlations were then used to evaluate monotonic relationships between the biofilm-component weights and the MP transport metrics.

Results

Biofilm morphogenesis in porous media

During the experiments, *B. subtilis* biofilms grew from isolated surface-attached clusters to a mature bio-clogged structure. Based on the observed morphology and the corresponding normalized-intensity distributions, we identify four representative stages of biofilm development: initial attachment, streamer formation,

transition to mature biofilm, and PFP formation.

At the initial stage ($t = 1.25\,\mathrm{h}$, Figure 2(a)), small bacterial clusters were distributed along the pillar surfaces. Most of the pore space, however, remained unoccupied. This is reflected in the normalized-intensity distribution, which contains a dominant peak near $I_s = 1$, corresponding primarily to regions with little or no biofilm.

At $t = 4\,\mathrm{h}$ (Figure 2(b)), the attached biomass elongated in the flow direction and formed filamentous streamers, consistent with previous observations of flow-induced streamer formation.[27] The dominant peak near $I_s = 1$ remained, but its relative contribution decreased and the distribution broadened over a wider range of intensities. This broadening reflects increasing morphological heterogeneity as streamers extended across the pore space.[40,41]

As biofilm growth continued, the streamers thickened and gradually transitioned into more continuous attached biofilm (Figure 2(c)).[42] At $t = 40\,\mathrm{h}$, the intensity distribution shifted toward lower values, consistent with greater coverage by optically dense biofilm within the pore space. At the same time, distinct filamentous streamer structures became less prominent.

At the final stage ($t = 64\,\mathrm{h}$, Figure 2(d)), the biofilm occupied most of the porous region and a persistent PFP formed between the inlet and outlet, consistent with previous observations in the same porous geometry.[15] The normalized-intensity distribution was dominated by low-intensity values, indicating extensive coverage by optically dense biofilm. The overall biofilm morphology became quasi-stationary at later times, although local growth and detachment continued (Video S1, Supporting Information).[16] Overall, biofilm development transformed the initially open pore network into a heterogeneous bioclogged structure containing a persistent PFP.

Quantification of biofilm morphological evolution

In this section, we quantify the relative contributions of different biofilm structures to the overall morphology. Previous studies have related normalized pixel intensity to biofilm density and permeability.[16] Based on the distribution of normalized pixel intensity, we model the intensity distribution at time t as a mixture of four Gaussian components. By comparing the fitted components with the corresponding images, we interpret these components as optical-intensity classes associated primarily with void space, streamers, and two biofilm-associated optical components with progressively lower characteristic intensities, respectively. Since these classifications are based on transmitted-light intensity, they should be interpreted as morphological indicators rather than direct measurements of biomass density.

The dashed lines in Panel II of Figure 2 show the fitted Gaussian components at representative times.

Consistent with the stage descriptions, the initial stage was dominated by the void-space component, while the contributions from the other components were negligible. During the streamer stage, a distinct streamer-associated component emerged and increased in weight, accompanied by a decrease in the void-space component. As the biofilm matured, the streamer-associated component decreased, while two biofilm-associated optical components increased. At the PFP stage, the intensity distribution became nearly unchanged and was dominated by the two biofilm-associated optical components. These representative distributions show the shift from an initially open pore space to streamer-dominated and, eventually, mature bioclogged conditions.

We further quantified this evolution from the temporal changes in the Gaussian-component weights (Figure 3). The streamer-associated component increased rapidly during the early stage ($t < 10$ h), accompanied by a sharp decrease in the void-space component. As time progressed, the void-space component continued to decrease, while the contributions from the two biofilm-associated optical components increased. At approximately $t = 25$ h, the void-space component had decreased substantially, and the streamer-associated component began to decline as streamers transitioned into attached biofilm. At later times, the streamer-associated component became small, while the two biofilm-associated optical components accounted for most of the intensity distribution. Similar trends were observed across independent experimental replicates (Figure S1).

Interestingly, the weights of the two biofilm-associated optical components remained approximately constant at later times, indicating that the system approached a quasi-stationary morphology. Local biofilm growth and detachment continued, but produced little change in the overall intensity distribution.[16] Overall, the Gaussian-mixture analysis quantifies the temporal transition from an initially open pore network to streamer-dominated and mature bioclogged conditions.

Interactions between biofilm morphology and microplastic transport

To better understand the effects of biofilm development on microplastic transport, fluorescent microplastics were injected at different stages of biofilm growth. The biofilm-component weights and MP transport metrics for all injection conditions are summarized in Table S2 of the Supporting Information. Here, we focus on the streamer-rich and PFP stages because they exhibit distinctly different biofilm morphologies and pore-scale structures.

We observed that microplastic transport changed significantly as biofilm morphology evolved. During the streamer-rich stage, MPs followed distributed paths through the pore space and frequently encountered filamentous biofilm structures (Figure 4(a); Video S2, Supporting Information). Some particles were temporarily retained near streamers, while others remained at the same locations after the injection, indi-

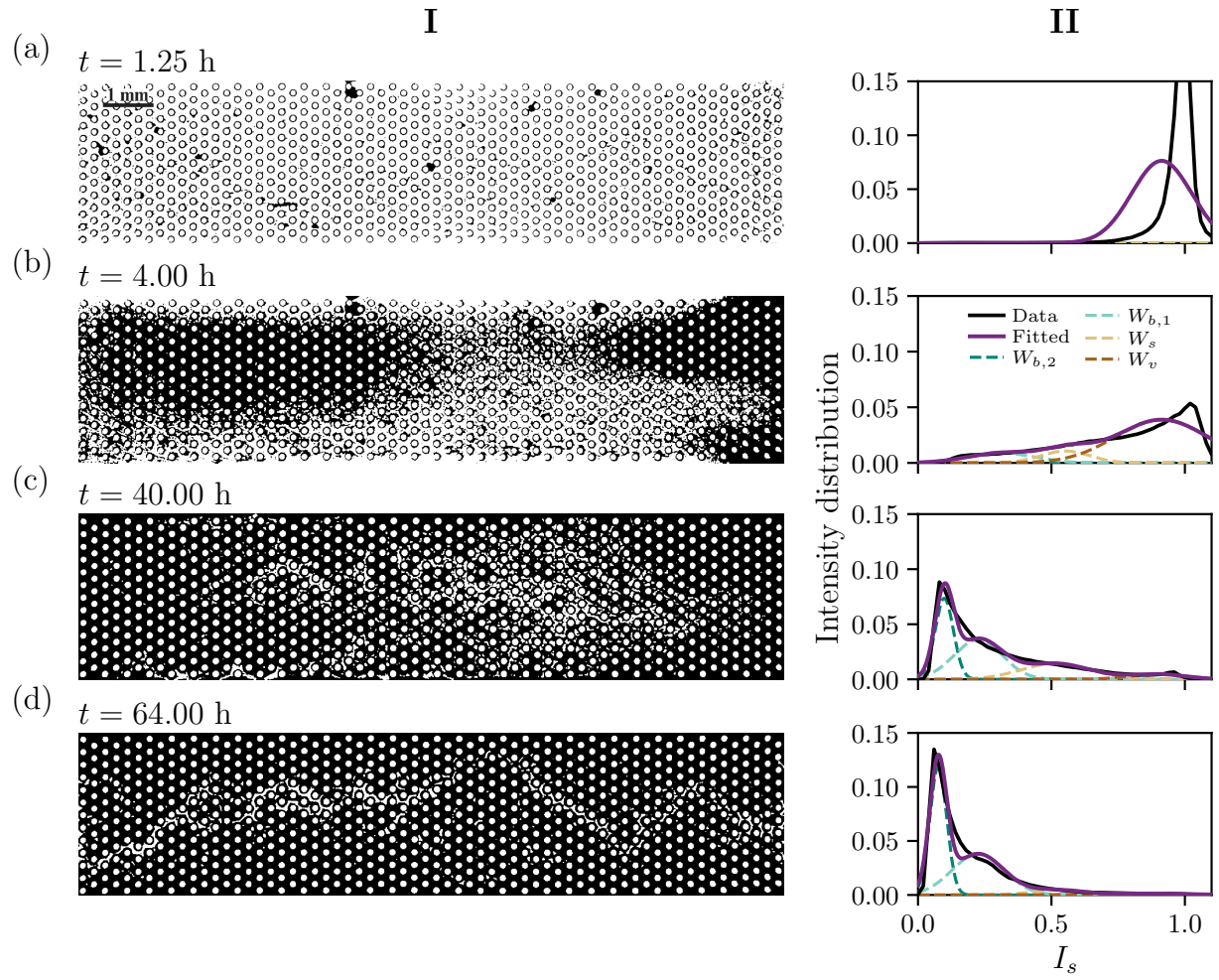

Figure 2: Temporal evolution of biofilm morphology and the corresponding normalized transmitted-light intensity distributions. Panel I shows representative biofilm images at (a) 1.25 h, (b) 4.00 h, (c) 40.00 h, and (d) 64.00 h, corresponding to initial attachment, streamer formation, biofilm maturation, and PFP formation, respectively. Panel II shows the measured intensity distributions (black), four-component Gaussian fits (purple), and individual fitted components (dashed lines). Flow is from left to right.

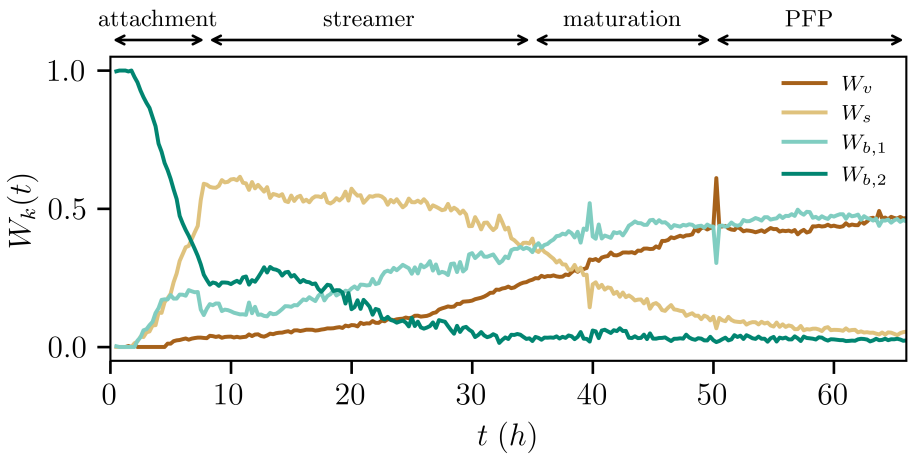

Figure 3: Temporal evolution of the four fitted optical-component weights during biofilm development in a representative experiment. W_v and W_s denote the void-space- and streamer-associated components, respectively, whereas $W_{b,1}$ and $W_{b,2}$ represent biofilm-associated optical components. The arrows indicate the representative attachment, streamer, maturation, and PFP stages identified from the corresponding images.

cating that their retention persisted beyond the injection period. Similar interactions between biofilms and microplastics have been reported previously without discussing the role of streamers.[20,43,44]

In contrast, microplastic transport during the PFP stage was concentrated within connected PFPs (Figure 4(b); and Video S3, Supporting Information). Few particles interacted with the biofilm, and almost no particles remained trapped after passing through the porous region. These observations indicate that the formation of a PFP reduces particle-biofilm interactions and limits microplastic trapping under the conditions investigated.

Figure 4(c) shows the probability density functions (PDFs) of the normalized retention time of non-trapped MPs, with color indicating the streamer-associated component weight W_s at the time of injection. At low W_s, the distribution was concentrated at short normalized retention times, consistent with rapid transport through PFPs. As W_s increased, the short-time peak decreased and the distribution broadened toward longer retention times. The corresponding CCDFs show that streamer-rich conditions resulted in a substantially larger fraction of particles with prolonged retention (Figure 4(d)), with the distributions decaying more slowly over time. In contrast, the CCDFs at low W_s decreased rapidly, indicating that most non-trapped MPs passed through the observation region over relatively short timescales. The retention-time distributions for all injection cases are provided in Figure S4 of the Supporting Information. Overall, biofilm morphology affected not only the retention-time distribution but also the fraction of MPs experiencing delayed transport.

Besides delayed MP transport, a small fraction of MPs remained trapped within the porous medium after

each injection. The maximum trapped fraction was approximately 4%. Although this fraction was small, the trapped MPs represented a distinct population because they remained immobilized over the observation period. Such persistent retention could contribute to MP accumulation in biofilm-colonized porous media under repeated particle loading.

To quantify the relationship between biofilm morphology and MP transport across all injection conditions, Figure 5 compares the mean normalized retention time ($\langle\tau_r\rangle/\tau_{PFP}$) and trapped fraction with both the streamer-associated component weight (W_s) and the total biofilm-associated component weight ($W_b = 1 - W_v$). Both the mean normalized retention time and the trapped fraction increased significantly with increasing W_s ($r_s = 0.92$, $p = 0.0002$ for retention time; $r_s = 0.87$, $p = 0.0012$ for trapped fraction). In contrast, neither metric showed a significant monotonic relationship with W_b ($r_s = -0.35$, $p = 0.328$ for retention time; $r_s = -0.41$, $p = 0.244$ for trapped fraction). These results indicate that MP transport was more strongly associated with biofilm morphology than with the overall biofilm-associated optical fraction.

Discussion

Previous studies have shown that biofilms can alter particle transport in porous media through changes in surface interactions, pore geometry, and local hydrodynamics.[18,45] Our results further show that these effects depend on the biofilm morphology within the pore space. Streamer-rich conditions were associated with longer MP retention times and greater trapping, whereas continued biofilm growth resulted in PFPs through which MPs were transported more rapidly. Thus, increasing biofilm accumulation did not result in a monotonic increase in MP retention. Instead, the dominant transport behavior changed as biofilm morphology evolved.

During the streamer-rich stage, filamentous biofilm structures extended into the pore space and increased the biofilm-fluid interface encountered by MPs. As a result, MPs were transported over a broader portion of the pore space instead of being concentrated within a single connected pathway. Under these conditions, the retention-time distributions broadened and developed longer tails, indicating that a larger fraction of non-trapped MPs experienced delayed transport. These observations suggest that streamers altered the spatial pathways and, consequently, the transport times of MPs: a fraction of MPs passed through relatively open regions and had shorter retention times, whereas others interacted with streamers and were retained for longer periods. In addition, a smaller fraction became trapped within the biofilm and remained immobilized over substantially longer times. These trapped MPs were typically embedded within the biofilm and remained immobilized unless local biofilm detachment occurred. Although the trapped fraction remained approximately 4% under the conditions investigated, such persistent retention may contribute to gradual

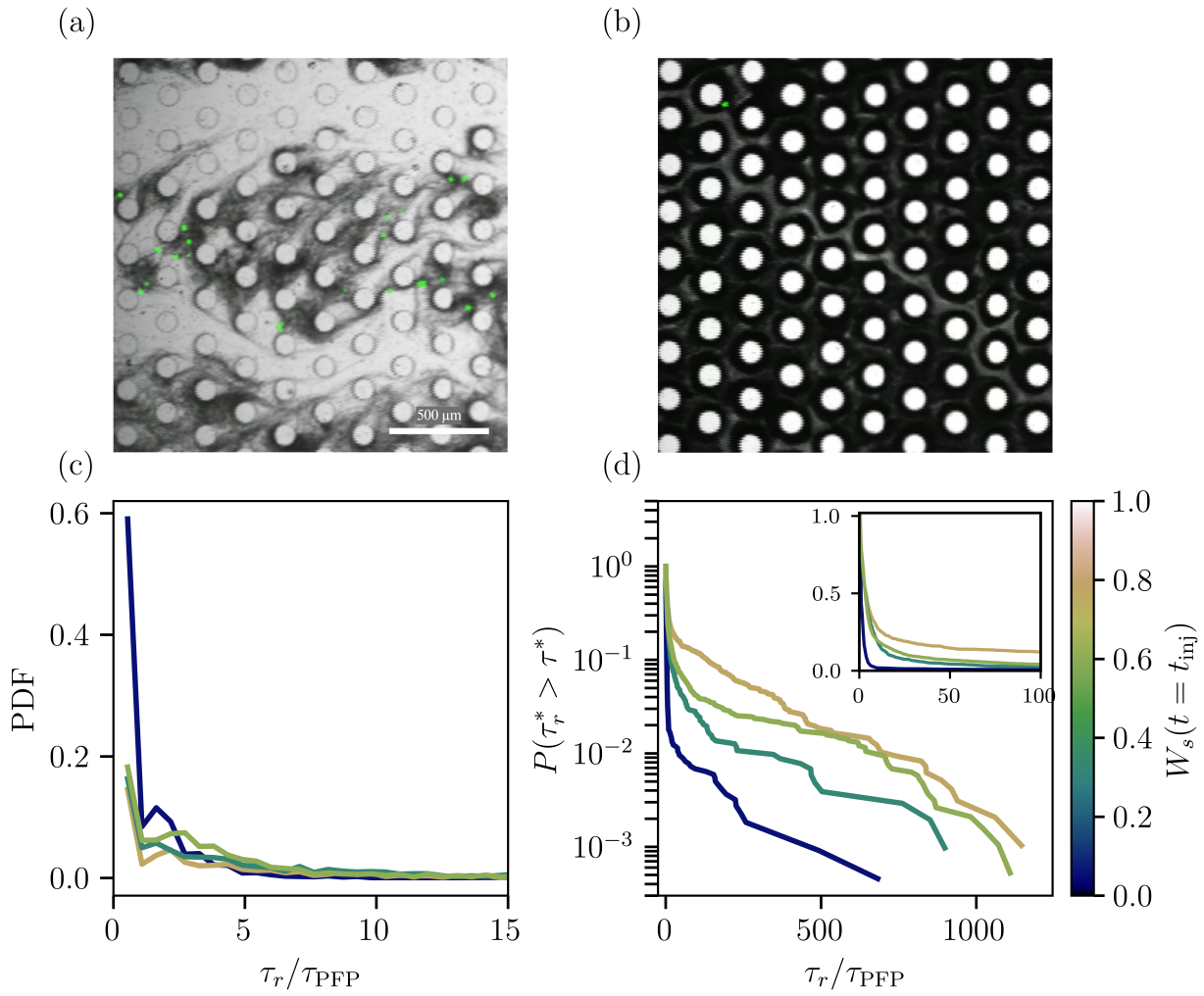

Figure 4: Microplastic transport under contrasting biofilm morphologies. Representative MP distributions during (a) streamer-rich and (b) PFP conditions, where green markers indicate detected MPs. (c) Probability density functions of normalized retention time, $\tau_r/\tau_{\mathrm{PFP}}$, for non-trapped MPs at selected streamer-associated component weights. (d) Corresponding complementary cumulative distributions over the full retention-time range with inset showing the early-time behavior for $0 \leq \tau_r/\tau_{\mathrm{PFP}} \leq 100$. Line color indicates W_s at the time of MP injection.

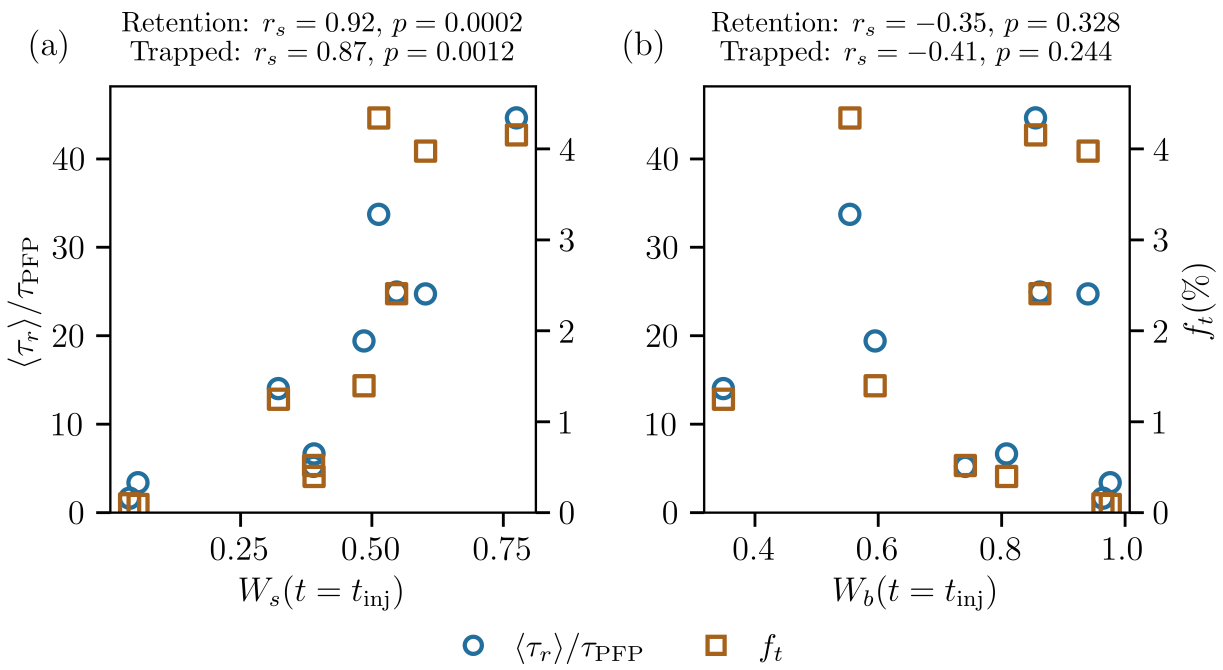

Figure 5: Relationships between biofilm morphology and MP transport. Mean normalized retention time ($\langle \tau_r \rangle / \tau_{\mathrm{PFP}}$)and trapped fraction ($f_t$) are shown as functions of (a) the streamer-associated component weight W_s and (b) the total biofilm-associated component weight $W_b = 1 - W_v$. Spearman rank correlation coefficients (r_s) and corresponding p values are reported for both transport metrics in each panel.

MP accumulation under repeated loading. Unlike dissolved solutes that primarily follow advective pathways, MPs can also interact with and become trapped by biofilms, making their interaction with evolving pore-scale flow pathways dependent on biofilm morphology.

In contrast to the streamer-rich stage, prolonged biofilm growth resulted in a different transport regime. As the porous medium became bioclogged, flow was increasingly channeled into a connected PFP, reducing particle-biofilm interaction and therefore promoting rapid MP transport. The retention-time distributions were concentrated at short retention times, although a small number of MPs occasionally experienced much longer retention, and the trapped fraction remained low. Our findings are consistent with previous studies showing that bioclogging can redistribute flow and generate preferential transport pathways in porous media.[15–18] Once a connected PFP develops, MPs may therefore bypass most of the biofilm-colonized pore space and migrate farther downstream rather than being locally retained.

The relationships across all conditions further support the importance of biofilm morphology. The streamer-associated component weight, W_s, was strongly correlated with both the mean normalized retention time and the trapped fraction ($r_s = 0.92$, $p = 0.0002$ for retention time; $r_s = 0.87$, $p = 0.0012$ for trapped fraction). In contrast, neither transport metric showed a significant monotonic relationship with

the total biofilm-associated component weight, W_b. Thus, biofilm accumulation alone did not explain the observed differences in MP transport. Instead, streamer development was more positively correlated with particle delay and trapping. A pore space containing extensive biofilm growth (bioclogged) can therefore exhibit rapid MP transport when flow is focused through a connected PFP, whereas a less bioclogged but streamer-rich pore space can produce longer retention and more spatially distributed transport.

Environmental Implications

The observed transition from streamer-rich to PFP-dominated transport reveals a pore-scale mechanism by which biofilm development can alter MP transport non-monotonically over time. Streamer-rich biofilms promoted spatially distributed and delayed transport, whereas continued bioclogging generated a connected PFP that enabled more rapid MP transport. These findings imply that predicting MP transport in heterogeneous subsurface environments requires accounting for spatial and temporal variations in biofilm morphology and the degree of bioclogging. Regions with similar biofilm accumulation may therefore exhibit different transport behavior depending on whether biofilms form streamers or redirect flow into preferential pathways. This variability complicates predictions of where MPs will be retained or bypass biofilm-colonized regions, and may affect estimates of their downstream migration and accumulation.

Predictive models that represent biofilm effects through a single, constant retardation factor may not capture transitions among delayed, trapped, and preferential-flow transport regimes as biofilms develop. Such uncertainty can also limit the ability to predict MP removal or retention in engineered and natural treatment systems that are based on porous media. Future studies should examine whether these relationships persist across different pore geometries, bacterial strains, MP sizes and surface properties, and flow conditions, and determine how these factors modify the transition between streamer-rich and PFP-dominated transport.

Acknowledgements

We thank Ge Zhang for assistance with the microfluidic device design and fabrication. We also thank Dr. Kung-Hui Chu (Bella) and Jooho Chung for providing the *Bacillus subtilis* strain.

Supporting Information

Additional information on biofilm-growth experiments, particle-tracking validation and sensitivity analysis, microplastic-injection conditions, and retention-time distributions (PDF); supplementary videos of biofilm

development and microplastic transport (MP4).

References

[1] Chen, J.; Wu, J.; Sherrell, P. C.; Chen, J.; Wang, H.; Zhang, W.; Yang, J. How to Build a Microplastics-Free Environment: Strategies for Microplastics Degradation and Plastics Recycling. *Advanced Science* **2022**, *9*, 2103764.

[2] Geyer, R.; Jambeck, J. R.; Law, K. L. Production, use, and fate of all plastics ever made. *Science Advances* **2017**, *3*, e1700782.

[3] Cole, M.; Lindeque, P.; Halsband, C.; Galloway, T. S. Microplastics as contaminants in the marine environment: A review. *Marine Pollution Bulletin* **2011**, *62*, 2588–2597.

[4] Ragoobur, D.; Huerta-Lwanga, E.; Somaroo, G. D. Microplastics in agricultural soils, wastewater effluents and sewage sludge in Mauritius. *Science of The Total Environment* **2021**, *798*, 149326.

[5] Carpanez, T. G.; Castro, L. M. C.; Amaral, M. C. S.; Moreira, V. R. Occurrence and environmental consequences of microplastics and nanoplastics from agricultural reuse of wastewater and biosolids in the soil ecosystem: A review. *Science of The Total Environment* **2025**, *980*, 179538.

[6] Wu, J.-y.; Gao, J.-m.; Pei, Y.-z.; Luo, K.-y.; Yang, W.-h.; Wu, J.-c.; Yue, X.-h.; Wen, J.; Luo, Y. Microplastics in agricultural soils: A comprehensive perspective on occurrence, environmental behaviors and effects. *Chemical Engineering Journal* **2024**, *489*, 151328.

[7] Yuan, P.; Cao, X.; Zhao, L.; Xu, X.; Romero-Freire, A.; Qiu, H. Overlooked yet critical pathways for microplastics input to soil and groundwater system: Transport mechanisms and simulation predictions in landfill environments. *Water Research* **2025**, *284*, 124041.

[8] Hechmi, S.; Bhat, M. A.; Kallel, A.; Khiari, O.; Louati, Z.; Khelil, M. N.; Zoghlami, R. I.; Cherni, Y.; Melki, S.; Trabelsi, I.; Jedidi, N. Soil contamination with microplastics (MPs) from treated wastewater and sewage sludge: risks and sustainable mitigation strategies. *Discover Environment* **2024**, *2*, 95.

[9] Hussain, K.; Fox, J.-P.; Ma, X.; Rossi, L. Impact of polystyrene nanoplastics on physiology, nutrient uptake, and root system architecture of aeroponically grown citrus plants. *NanoImpact* **2025**, *37*, 100536.

[10] Nizzetto, L.; Bussi, G.; Futter, M. N.; Butterfield, D.; Whitehead, P. G. A theoretical assessment of microplastic transport in river catchments and their retention by soils and river sediments. *Environmental Science: Processes & Impacts* **2016**, *18*, 1050–1059.

[11] Okutan, H.; Sağır, c.; Kurtuluş, B.; Özmen, H. B.; Pekkan, E.; Razack, M.; Le Coustumer, P. Numerical and Experimental Approach to Evaluate Microplastic Transport in Saturated Porous Media. *Microplastics* **2024**, *3*, 463–476.

[12] Zeng, L.; Yuan, C.; Xiang, T.; Guan, X.; Dai, L.; Xu, D.; Yang, D.; Li, L.; Tian, C. Research on the Migration and Adsorption Mechanism Applied to Microplastics in Porous Media: A Review. *Nanomaterials* **2024**, *14*, 1060.

[13] Meng, Q.; Shi, F.; Fan, W.; Wen, Z.; Sun, K.; Wang, Z. SiO2 and microparticle transport in a saturated porous medium: effects of particle size and flow rate. *Applied Water Science* **2024**, *14*, 50.

[14] Li, W.; Brunetti, G.; Bolshakova, A.; Stumpp, C. Effect of particle density on microplastics transport in artificial and natural porous media. *Science of The Total Environment* **2024**, *935*, 173429.

[15] Kurz, D. L.; Secchi, E.; Carrillo, F. J.; Bourg, I. C.; Stocker, R.; Jimenez-Martinez, J. Competition between growth and shear stress drives intermittency in preferential flow paths in porous medium biofilms. *Proceedings of the National Academy of Sciences* **2022**, *119*, e2122202119.

[16] Kurz, D. L.; Secchi, E.; Stocker, R.; Jimenez-Martinez, J. Morphogenesis of Biofilms in Porous Media and Control on Hydrodynamics. *Environmental Science & Technology* **2023**, *57*, 5666–5677.

[17] Bottero, S.; Storck, T.; Heimovaara, T. J.; Van Loosdrecht, M. C.; Enzien, M. V.; Picioreanu, C. Biofilm development and the dynamics of preferential flow paths in porous media. *Biofouling* **2013**, *29*, 1069–1086.

[18] Carrel, M.; Morales, V. L.; Dentz, M.; Derlon, N.; Morgenroth, E.; Holzner, M. Pore-Scale Hydrodynamics in a Progressively Bioclogged Three-Dimensional Porous Medium: 3-D Particle Tracking Experiments and Stochastic Transport Modeling. *Water Resources Research* **2018**, *54*, 2183–2198.

[19] Jiao, W.; Scheidweiler, D.; Delouche, N.; Guadagnini, A.; de Anna, P. Spatial Organization of Biomass Controls Intrinsic Permeability of Porous Systems. *Environmental Science & Technology* **2026**, *60*, 15952–15963.

[20] He, L.; Rong, H.; Wu, D.; Li, M.; Wang, C.; Tong, M. Influence of biofilm on the transport and deposition behaviors of nano- and micro-plastic particles in quartz sand. *Water Research* **2020**, *178*, 115808.

[21] Liu, Y.; Yang, C.-H.; Li, J. Adhesion and Retention of a Bacterial Phytopathogen Erwinia chrysanthemi in Biofilm-Coated Porous Media. *Environmental Science & Technology* **2008**, *42*, 159–165.

[22] Mitzel, M. R.; Sand, S.; Whalen, J. K.; Tufenkji, N. Hydrophobicity of biofilm coatings influences the transport dynamics of polystyrene nanoparticles in biofilm-coated sand. *Water Research* **2016**, *92*, 113–120.

[23] Wei, G.; Yang, J. Q. Biofilm-induced microplastic transport under subcritical shear stress. *Water Research* **2026**, *298*, 125818.

[24] Scheidweiler, D.; Peter, H.; Pramateftaki, P.; de Anna, P.; Battin, T. J. Unraveling the biophysical underpinnings to the success of multispecies biofilms in porous environments. *The ISME Journal* **2019**, *13*, 1700–1710.

[25] Drescher, K.; Shen, Y.; Bassler, B. L.; Stone, H. A. Biofilm streamers cause catastrophic disruption of flow with consequences for environmental and medical systems. *Proceedings of the National Academy of Sciences* **2013**, *110*, 4345–4350.

[26] Taherzadeh, D.; Picioreanu, C.; Horn, H. Mass Transfer Enhancement in Moving Biofilm Structures. *Biophysical Journal* **2012**, *102*, 1483–1492.

[27] Rusconi, R.; Lecuyer, S.; Guglielmini, L.; Stone, H. A. Laminar flow around corners triggers the formation of biofilm streamers. *Journal of The Royal Society Interface* **2010**, *7*, 1293–1299.

[28] Rusconi, R.; Lecuyer, S.; Autrusson, N.; Guglielmini, L.; Stone, H. Secondary Flow as a Mechanism for the Formation of Biofilm Streamers. *Biophysical Journal* **2011**, *100*, 1392–1399.

[29] Wagner, M.; Horn, H. Optical coherence tomography in biofilm research: A comprehensive review. *Biotechnology and Bioengineering* **2017**, *114*, 1386–1402.

[30] Zhang, M.; Zhang, J.; Wang, Y.; Wang, J.; Achimovich, A. M.; Acton, S. T.; Gahlmann, A. Non-invasive single-cell morphometry in living bacterial biofilms. *Nature Communications* **2020**, *11*, 6151.

[31] Li, M.; Nahum, Y.; Matouš, K.; Stoodley, P.; Nerenberg, R. Effects of biofilm heterogeneity on the apparent mechanical properties obtained by shear rheometry. *Biotechnology and bioengineering* **2023**, *120*, 553–561.

[32] Li, M.; Perez-Calleja, P.; Kim, B.; Picioreanu, C.; Nerenberg, R. Unique stratification of biofilm density in heterotrophic membrane-aerated biofilms: An experimental and modeling study. *Chemosphere* **2023**, *327*, 138501.

[33] Wei, G.; Yang, J. Q. Microfluidic investigation of the impacts of flow fluctuations on the development of Pseudomonas putida biofilms. *npj Biofilms and Microbiomes* **2023**, *9*, 73.

[34] Zhang, J.; Zhang, M.; Wang, Y.; Donarski, E.; Gahlmann, A. Optically Accessible Microfluidic Flow Channels for Noninvasive High-Resolution Biofilm Imaging Using Lattice Light Sheet Microscopy. *The Journal of Physical Chemistry B* **2021**, *125*, 12187–12196.

[35] Dykes, C.; Pearson, J. M.; Bending, G. D.; Abolfathi, S. Biofilm growth is insufficient to retain large buoyant microplastics in constructed wetlands. *Journal of Hazardous Materials* **2026**, *504*, 141265.

[36] Hamon, M. A.; Stanley, N. R.; Britton, R. A.; Grossman, A. D.; Lazazzera, B. A. Identification of AbrB-regulated genes involved in biofilm formation by *Bacillus subtilis*. *Molecular Microbiology* **2004**, *52*, 847–860.

[37] Valiei, A.; Kumar, A.; Mukherjee, P. P.; Liu, Y.; Thundat, T. A web of streamers: biofilm formation in a porous microfluidic device. *Lab on a Chip* **2012**, *12*, 5133.

[38] Sharipova, M.; Rudakova, N.; Mardanova, A.; Evtugyn, V.; Akosah, Y.; Danilova, I.; Suleimanova, A. Biofilm Formation by Mutant Strains of Bacilli under Different Stress Conditions. *Microorganisms* **2023**, *11*, 1486.

[39] Ouellette, N. T.; Xu, H.; Bodenschatz, E. A quantitative study of three-dimensional Lagrangian particle tracking algorithms. *Experiments in Fluids* **2006**, *40*, 301–313.

[40] Hall-Stoodley, L.; Costerton, J. W.; Stoodley, P. Bacterial biofilms: from the Natural environment to infectious diseases. *Nature Reviews Microbiology* **2004**, *2*, 95–108.

[41] Krsmanovic, M.; Biswas, D.; Ali, H.; Kumar, A.; Ghosh, R.; Dickerson, A. K. Hydrodynamics and surface properties influence biofilm proliferation. *Advances in Colloid and Interface Science* **2021**, *288*, 102336.

[42] Savorana, G.; Słomka, J.; Stocker, R.; Rusconi, R.; Secchi, E. A microfluidic platform for characterizing the structure and rheology of biofilm streamers. *Soft Matter* **2022**, *18*, 3878–3890.

[43] Al Harraq, A.; Bharti, B. Microplastics through the Lens of Colloid Science. *ACS Environmental Au* **2022**, *2*, 3–10.

[44] Pete, A. J.; Brahana, P. J.; Bello, M.; Benton, M. G.; Bharti, B. Biofilm Formation Influences the Wettability and Settling of Microplastics. *Environmental Science & Technology Letters* **2023**, *10*, 159–164.

[45] Leon Morales, C. F.; Strathmann, M.; Flemming, H.-C. Influence of biofilms on the movement of colloids in porous media: Implications for colloid facilitated transport in subsurface environments. *Water Research* **2007**, *41*, 2059–2068.